

Received November 5, 2019, accepted November 18, 2019, date of publication November 21, 2019, date of current version December 9, 2019.

Digital Object Identifier 10.1109/ACCESS.2019.2954935

Technology of Actual Wind Deviation Monitoring for Suspension Insulator Strings Based on Improved Edge Detection

LUYA YANG¹, XINBO HUANG^{1,2}, (Senior Member, IEEE),

YE ZHANG^{1,2}, AND TINGTING NIE²

¹School of Electro-Mechanical Engineering, Xidian University, Xi'an 710071, China

²School of Electronics and Information, Xi'an Polytechnic University, Xi'an 710048, China

Corresponding author: Xinbo Huang (huangxb1975@163.com)

This work was supported in part by the Shaanxi Industrial Science and Technology Tackling Key Problems Fund under Grant 2016GY-052, and in part by the Project of Science and Technology Research of Shaanxi under Grant 2018ZDXM-GY-040 and Grant 2018JQ5049.

ABSTRACT Finding out the wind deviation fault of the insulators of transmission lines in time can not only help people better complete the wind bias warning and prevention work, but also reduce the economic loss and the maintenance difficulty. A technology of Actual Wind Deviation Monitoring for Suspension Insulator Strings Based on Improved Edge Detection is proposed in this paper. It can calculate the actual wind deviation angle and distance of the insulator through image processing technology and camera calibration. Firstly, the video monitoring device is installed on the tower to collect the field insulator images, and the R + G improved grayscale processing and median filtering are carried out. Secondly, two-dimensional Otsu threshold segmentation is applied to the pre-processed image, and the insulator string target is obtained by combining morphological filtering and connection domain extraction. Then, the improved Kirsch operator is used to obtain the complete single-pixel wide edge of the insulator string. Searching the left and right boundary points of each insulator separately and the center points of each insulator can be calculated. Finally, these center points are transformed into world coordinates by camera calibration and fitted by least square method (LSM). The deviation angle θ of the insulator string can be obtained according to the slope of the fitting line, and the deviation distance d according to the length of the insulator string. When θ is greater than 7.5° and d is greater than 300mm, an alarm is issued to alert the staff. We analyze the performance of the technology by a series of experiments, the maximum error between the proposed method and the manual method is 8.72% and the minimum is 1.01%. Moreover, by analyzing 200 field insulator images, the identification accuracy are 93.75% and 91.36% respectively, which shows that the proposed method is effective and practical. It provides a new idea for the wind deviation monitoring of suspension insulator strings.

INDEX TERMS Insulator wind deviation, improved gray processing, improved Kirsch operator, camera calibration, deviation angle and distance.

I. INTRODUCTION

In recent years, wind flashover accidents on transmission lines have occurred frequently, which has seriously threatened the safe operation of the power grid and caused significant economic losses [1], [2]. Moreover, after the accident, it is difficult to determine the location of the fault, which brings great trouble to the maintenance work [3], [4].

The associate editor coordinating the review of this manuscript and approving it for publication was Lefei Zhang¹.

Therefore, monitoring the wind deviation of transmission lines is particularly important [5].

The wind deviation of suspension insulators is the inclination angle of the insulator string relative to the tower under the action of the wind, which is the most important factor causing the wind-biased trip accident. At present, the commonly used insulator wind deviation monitoring method mainly uses the tilt sensor for detection [6], or simplifying the insulator to establish a rigid straight rod model and using the wind deviation formula to calculate the deviation angle [7].

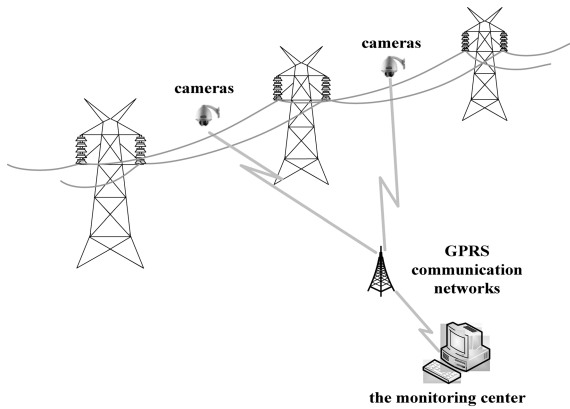


FIGURE 1. Block diagram of the online monitoring system.

On the one hand, these methods require complex mechanical analysis, and the amount of calculation is large. On the other hand, due to sensor accuracy or mathematical model constraints, all factors affecting the wind deviation cannot be taken into account and there will be certain errors. In order to monitor the wind deviation angle and distance of the insulator string more intelligently, the measurement technology proposed in this paper uses the video monitoring device to collect the insulator string images, and based on the analysis of the wind bias characteristics of the insulator, the image processing techniques are used [8]–[11]. An improved grayscale method is proposed to improve the contrast between the insulator and the background. And an improved Kirsch operator is proposed to obtain the complete single-pixel wide insulator string edge. The center point of each insulator is calculated and fitted to obtain the axis of the insulator string, and the wind deviation angle and distance can be calculated. The method can realize non-contact online monitoring and provides a new idea for wind deviation monitoring of transmission lines.

II. OVERVIEW OF THE TECHNOLOGY OF THE WIND DEVIATION MONITORING

A. FRAMEWORK OF WIND DEVIATION MONITORING TECHNOLOGY

The proposed measurement technology consists of three parts: the monitoring device with image sensors, the GPRS communication networks [12], [13] and the monitoring center with the insulator wind deviation analysis software. The insulator images are captured by image sensors, decompressed and sent to the monitoring center by GPRS communication networks, then analyzed by the proposed algorithms. The block diagram of the monitoring system is illustrated in Figure 1, which can realize the 24-hour online monitoring of UHV transmission lines [14], [15].

B. PRINCIPLE OF INSULATOR WIND DEVIATION MEASUREMENT

The wind deviation measurement flow chart of the insulator is shown in Figure 2. Firstly, the video monitoring device is installed on the tower, whose angle and position can be

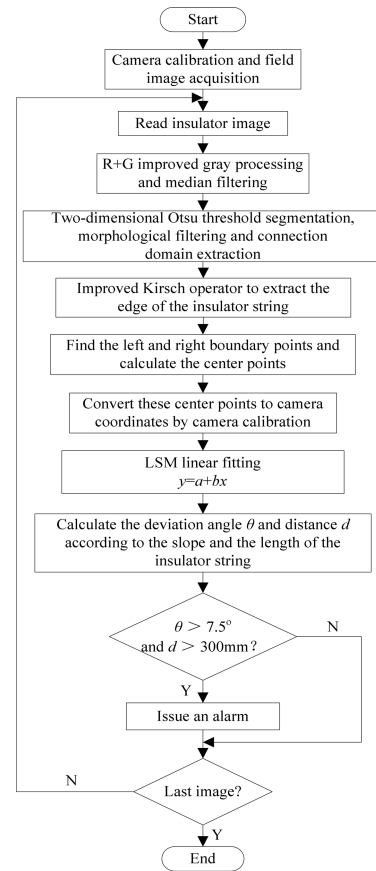


FIGURE 2. Wind deviation measurement flow chart.

adjusted to collect the field insulator images. The R + G improved grayscale processing is performed on the collected RGB color image, and the median filtering is used for denoising. Secondly, two-dimensional Otsu threshold segmentation is applied to the pre-processed image, and the insulator string target is obtained by combining morphological filtering and connection domain extraction. Then, the improved Kirsch operator is used to obtain the complete single-pixel wide edge of insulator strings, searching the left and right boundary points of each insulator separately. The center points of each insulator can be calculated. Finally, these center points are transformed into world coordinates by camera calibration and fitted by least square method. The deviation angle θ of insulator string can be obtained according to the slope of the fitting line, and the deviation distance d according to the length of the insulator string. When θ is greater than 7.5° and d is greater than 300mm, an alarm is issued to alert the staff to make corresponding maintenance, otherwise the insulator string is operating normally.

The insulator wind deviation model is shown in Figure 3. It can monitor the variation of the insulator deviation angle and distance. The insulator string axis calculation model is shown in Figure 4, the maximum value points of the left edge and the right edge of each insulator are respectively searched, that is, the left boundary points LP and the right

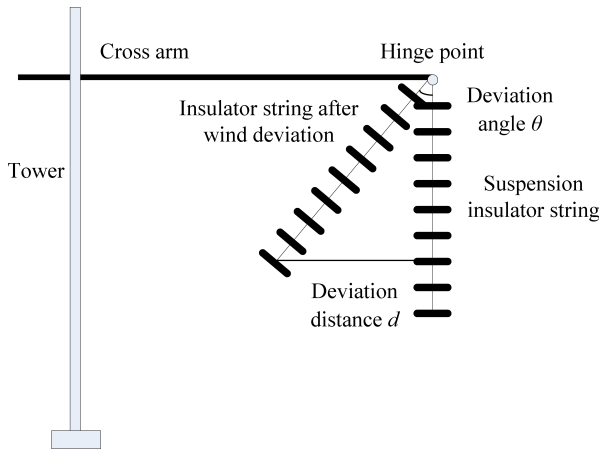


FIGURE 3. Wind deviation model.

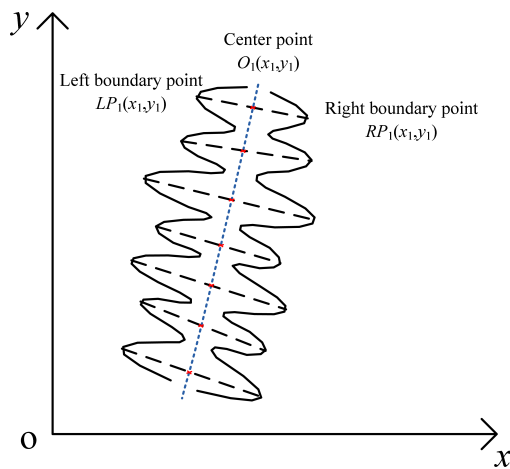


FIGURE 4. Insulator string axis calculation model.

boundary points RP . The midpoint of the line connecting the two boundary points is the center point O of the insulator, which is the red point in Figure 4. The center points of each insulator can be calculated in turn, which are converted into world coordinates by camera calibration and fitted, the axis of the insulator string can be obtained.

The deviation angle and distance of the insulator string are shown in Figure 5, the blue solid line is the fitted insulator string axis $y = a + bx$ and the length is L . The red dotted line indicates the ideal vertical direction of the insulator string, the angle between the blue solid line and the red dotted line is the deviation angle $\theta = 90^\circ - \arctan b$, and the blue dotted line indicates the horizontal deviation distance $d = L \sin \theta$.

III. INSULATOR STRING IDENTIFICATION

A. IMAGE PRE-PROCESSING

At present, the images acquired and displayed by the image collector are RGB color images, including R, G and B channels. R, G and B represent the gray values of red, green and blue pixels in the image. In the process of practical application, according to the color characteristics and processing purposes of the image, the corresponding color space

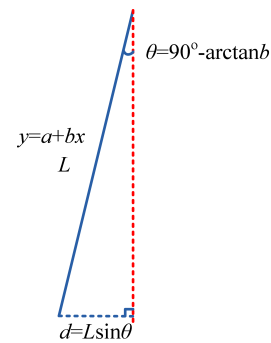


FIGURE 5. Deviation angle and distance of the insulator.

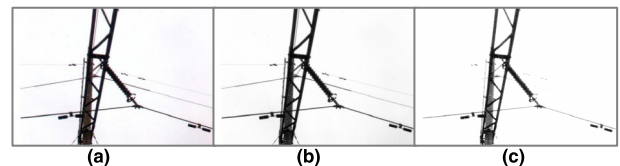


FIGURE 6. Grayscale processing. (a) original image. (b) grayscale. (c) improved grayscale.

conversion and grayscale processing are needed to reduce the amount of data and computation of the processing object. In [16], the insulator image is transformed into HSI color space, H and S components are processed respectively, and connected domain shape is used to identify insulator. But the processing effect of insulator image taken in dark weather is not good, and the algorithm processing speed is slow due to the conversion of color space. In [17], insulator image is directly weighted and grayed and the Otsu method is used to get the target. The processing speed is fast, but the processing effect of the insulator image with rich color and complex background is not ideal.

In view of the above problems, this paper proposes a R + G improved grayscale processing method based on red and green channels. Firstly, RGB color image channel decomposition is performed, and the formula is as follows:

$$Y = Rr + Gg + Bb \tag{1}$$

where Y represents a specific color, R represents the red color, G represents the green color and B represents the blue color. r represents the proportion coefficient of the red color, g represents the proportion coefficient of the green color and b represents the proportion coefficient of the blue color. After getting the R, G, B channels of the image, the R channel and G channel are added R + G, which is the result of the improved grayscale processing method proposed in this paper. The contrast result of gray-scale processing for a field insulator image is shown in Figure 6, (b) is the result of the general grayscale processing, the contrast between insulator string and tower and conductor is not obvious, so it is difficult to extract the insulator target. While the contrast in (c) is enhanced by using improved grayscale processing, and the interference conductors near the insulator string are also removed,

TABLE 1. Comparison of grayscale methods.

Method	(1)	(2)	(3)	(4)	(5)
Original image					
Grayscale					
H-component					
R-B					
R+G in this paper					

which is advantageous for the subsequent segmentation and extraction of the insulator string.

In this paper, five field insulator string images (1)-(5) in different environments are selected, as shown in Table 1, using grayscale [18], H-component [19], R-B [20] and the R + G improved grayscale algorithm respectively.

The comparison results show that, the contrast between the insulator target and other targets such as conductors is not obvious by using grayscale method, and it is difficult to extract the insulator separately. The H component processing results have low contrast and the insulator target is fuzzy and incomplete. By R-B processing, the insulator target is integrated with the background, and it is difficult to achieve separation. The improved grayscale algorithm proposed in this paper can not only improve the contrast between the insulator and the background, but also eliminate the interference between the conductor and other targets, which is beneficial to the subsequent separation of the insulator target from the background.

In the process of digital image acquisition and transmission, due to the participation of hardware devices and the influence of external factors, mixed noise will be caused, which has a great influence on the image processing process. Therefore, median filtering [21], [22] is used for denoising. The result of the median filtering process is shown in Figure 7. After filtering, the details of the insulator region can be completely preserved and the noise points in the image can be well removed.

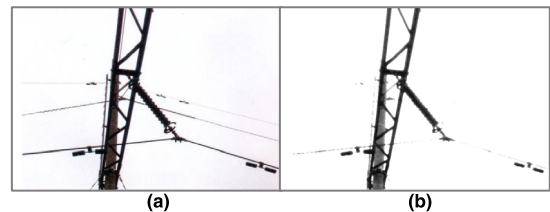


FIGURE 7. Image denoising. (a) original image. (b) median filtering.

B. INSULATOR STRING EXTRACTION AND EDGE DETECTION

1) INSULATOR STRING SEGMENTATION

The pre-processed insulator image is segmented to extract the insulator string target. The Otsu threshold segmentation method is the most commonly used algorithm, but its disadvantage is that it cannot reflect the spatial distribution between the pixels of the image, and is easily affected by noise and external factors, resulting in unsatisfactory segmentation effect. Therefore, this paper introduces the two-dimensional Otsu threshold segmentation method [23], which can well reflect the spatial distribution relationship of each pixel in the image, thus the noise existing in the image is avoided to disturb the segmentation effect, and the segmentation accuracy is improved.

Figure 8 is a schematic diagram of two-dimensional gray histogram. When a certain point is selected, the gray value is represented on the horizontal axis S, and the average gray value of all the pixels in the adjacent area of the point is

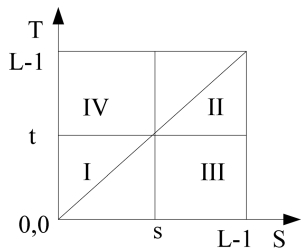


FIGURE 8. Two-dimensional gray histogram.

represented on the vertical axis T. The entire plane is divided into four regions, where region I represents the target, region II represents the background, region III represents the image boundary, and region IV represents the noise.

Suppose there are L gray values in an image, which are expressed as [1, 2, . . . , L]. The pixel to be processed is $f(m, n)$, the formula for calculating the average gray value in its adjacent area is:

$$mean(m, n) = \frac{1}{s * s} \sum_{i=-(s-1)/2}^{(s-1)/2} \sum_{j=-(s-1)/2}^{(s-1)/2} f(m+i, n+j) \tag{2}$$

where s represents the size of the adjacent area. The probability of occurrence of the target and background regions in the image are:

$$w_0 = \sum_{i=1}^s \sum_{j=1}^t P_{ij} = w_0(s, t) \tag{3}$$

$$w_1 = \sum_{i=s+1}^L \sum_{j=t+1}^L P_{ij} = w_1(s, t) \tag{4}$$

In the formula, P_{ij} represents the probability of occurrence of a certain gray level pixel point.

The two-dimensional average gray level of the two types is:

$$\mu_0 = (\mu_{0i}, \mu_{0j})^T = \left[\sum_{i=1}^s \sum_{j=1}^t ip_{ij}/w_0(s, t), \sum_{i=1}^s \sum_{j=1}^t jp_{ij}/w_0(s, t) \right]^T \tag{5}$$

$$\mu_1 = (\mu_{1i}, \mu_{1j})^T = \left[\sum_{i=s+1}^L \sum_{j=t+1}^L ip_{ij}/w_1(s, t), \sum_{i=s+1}^L \sum_{j=t+1}^L jp_{ij}/w_1(s, t) \right]^T \tag{6}$$

The two-dimensional average gray level after the combination of μ_0 and μ_1 is:

$$\mu_t = (\mu_{ti}, \mu_{tj})^T = \left[\sum_{i=0}^{L-1} \sum_{j=0}^{L-1} ip_{ij}, \sum_{i=0}^{L-1} \sum_{j=0}^{L-1} jp_{ij} \right]^T \tag{7}$$

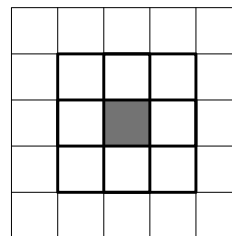


FIGURE 9. Eight connection domain.



FIGURE 10. Insulator extraction. (a) original image. (b) insulator segmentation.

Then the formula for maximum inter-class variance method is:

$$tr(\mu_B(S, T)) = w_0 [(\mu_{0i} - \mu_{ti})^2 + (\mu_{0j} - \mu_{tj})^2] + w_1 [(\mu_{1i} - \mu_{ti})^2 + (\mu_{1j} - \mu_{tj})^2] \tag{8}$$

When the variance $tr(\mu_B(s, t))$ is maximum, there is the following formula:

$$tr(\mu_B(s, t)) = \max \{tr(\mu_B(S, T))\} \tag{9}$$

Calculating the optimal threshold (s, t) is the desired two-dimensional segmentation threshold. The pre-processed insulator image is processed with the obtained threshold to obtain the insulator string, and the morphological filtering is combined to remove the hole inside the image. Since the image segmentation divides the image into many separate regions, not all regions are useful when analyzing the results. Therefore, connection domain extraction is needed to remove other interference regions. The eight connection domain is shown in Figure 9, it contains 8 pixels around a pixel, and the corresponding insulator string region can be finally obtained by marking the connection domain of the image and combining the area screening.

The result of segmentation and connection domain extraction of the insulator gray image is shown in Figure 10. Through morphological filtering and connection domain extraction, the holes in the target area and some pseudo-target small areas can be eliminated, and an insulator string image can be obtained that doesn't contain other targets.

In this paper, four field insulator string images (6)-(9) in different environments are selected, as shown in Table 2, pre-processing and image segmentation are performed. Finally, the complete separation of the insulator target from the background can be achieved and get the complete insulator string image.

TABLE 2. Results of insulator segmentation.

Segmentation	(6)	(7)	(8)	(9)
Original image				
Pre-processing				
Image segmentation				

5 5 5	3 5 5	-3 3 5	-3 -3 -3
3 0 -3	-3 0 5	-3 0 5	-3 0 5
-3 -3 3	-3 -3 -3	-3 -3 5	-3 5 5
-3 -3 -3	-3 -3 -3	5 -3 -3	5 5 3
-3 0 3	5 0 3	5 0 3	5 0 3
5 5 5	5 5 3	5 5 3	-3 -3 -3

FIGURE 11. Convolution template.

f_3	f_2	f_1
f_4	$f(x,y)$	f_0
f_5	f_6	f_7

FIGURE 12. Convolution operation result.

2) IMPROVED KIRSCH EDGE DETECTION ALGORITHM

After the insulator string is extracted, edge detection is required to obtain the edge of the insulator. In order to ensure the accuracy of edge detection and reduce the computational complexity of finding the maximum diameter of the insulator, this paper proposes an improved Kirsch edge detection algorithm. The principle is to incorporate refinement processing based on the traditional Kirsch edge detection operator to obtain the single-pixel wide and complete edge of the insulator string. The Kirsch edge detection operator [24], [25] consists of 8 convolution kernels, and the template is shown in Figure 11.

Each pixel in the image is convoluted with these 8 templates, as shown in Figure 12, the result of convolution operation of a certain pixel (x, y) with the above 8 templates is marked. Where $f(x, y)$ represents the gray value of the pixel point (x, y) , and f_0, f_1, \dots, f_7 represent the result of the convolution operation of (x, y) with the 8 templates respectively. Let $s_k = f_k + f_{k+1} + f_{k+2}$, $t_k = f_{k+3} + f_{k+4} + \dots + f_{k+7}$,

$k = 0, 1, \dots, 7$, then the gradient magnitude of the edge is:

$$K(x, y) = \max(1, \max(|5s_k - 4t_k|)) \quad (10)$$

If k in the formula exceeds 7, divide by 8 and take the remainder.

Then the refinement processing is operated, that is, the skeleton extraction [26]–[28]. The principle is to mark the edge points as 1 and the background points as 0. For all edge points in the image, using a 3×3 area to operate, as shown in Figure 13.

The first row of the skeleton extraction template is d_3, d_2 and d_9 , the second row is d_4, d_1 and d_8 , the third row is d_5, d_6 and d_7 . The point at the center is the center point d_1 . The center point d_1 is the edge point to be detected. If it satisfies: (1) $2 \leq N(d_1) \leq 6$, $N(d_1)$ is the number of non-zero neighbors of d_1 . (2) $S(d_1) = 1$, $S(d_1)$ is the number of times these values change from 0 to 1. (3) $d_2d_4d_6 = 0$ or $S(d_1) \neq 1$. (4) $d_4d_6d_8 = 0$ or $S(d_1) \neq 1$, then the d_1 is deleted. The algorithm iterates repeatedly until there is no point that satisfies the deletion condition, and a single-pixel wide edge line is obtained.

Edge detection is performed on a field insulator string image using Laplace operator, Canny operator and improved Kirsch operator respectively. The result is shown in Figure 14. The Laplace operator has partial edge loss. The Canny operator edge detection is complete, but not the single-pixel wide edge. in the subsequent edge maximum value search, the precision is low and the calculation amount is large. The improved Kirsch operator proposed in this paper can obtain a complete single-pixel wide edge of the insulator string.

IV. DEVIATION ANGLE AND DISTANCE CALCULATION OF THE INSULATOR STRING

A. CAMERA CALIBRATION

In the process of image measurement and location, in order to determine the relationship between the position of a point

d3	d2	d9
d4	d1	d8
d5	d6	d7

FIGURE 13. Skeleton extraction template.

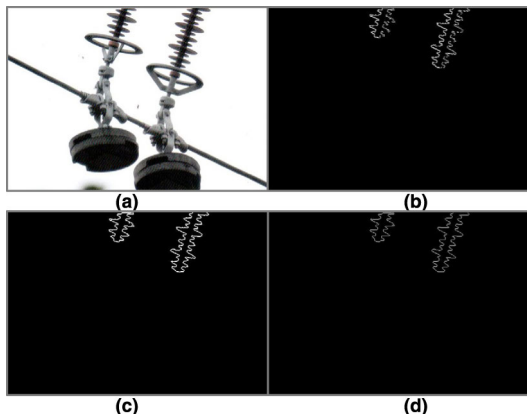


FIGURE 14. Edge detection results. (a) original image. (b) Laplace operator. (c) Canny operator. (d) improved Kirsch.

on the surface of a space object and its corresponding point in the image, the geometric model of the camera imaging must be established. The process of solving the geometric model parameters is the camera calibration [29]–[31]. The principle of camera calibration is as follows: Assume that the calibration plate plane is located on the plane of $Z = 0$ of the world coordinate system. The world coordinate of the feature points on the calibration plate is $A(x_w, y_w, 0)$, and the corresponding image coordinate is $a(u_w, v_w)$, which can be obtained as follows:

$$\varphi \begin{bmatrix} u_w \\ v_w \\ 1 \end{bmatrix} = M \begin{bmatrix} r_1 & r_2 & T \end{bmatrix} \begin{bmatrix} x_w \\ y_w \\ 1 \end{bmatrix} \quad (11)$$

where φ is the depth coefficient, M is the internal parameter of the camera, r_1 and r_2 are the rotation vectors, and T is the translation vector. $H = M \begin{bmatrix} r_1 & r_2 & T \end{bmatrix}$ is the rotation and translation vector of the world coordinate system relative to the image pixel coordinate system, that is, the homography matrix. The homography matrix H can be obtained by solving the equation. To define a matrix $E = M^{-T}M^{-1}$ can get the following formula:

$$\begin{cases} q_x = \sqrt{\mu/E_{11}} \\ q_y = \sqrt{\mu E_{11}/(E_{11}E_{22} - E_{12}^2)} \\ u_0 = \gamma v_0/q_x - E_{13}q_x^2/\mu \\ v_0 = (E_{12}E_{13} - E_{11}E_{23})/(E_{11}E_{22} - E_{12}^2) \\ \gamma = -E_{12}q_x^2q_y/\mu \\ \mu = E_{33} - [E_{13}^2 + v_0(E_{12}E_{13} - E_{11}E_{23})]/E_{11} \end{cases} \quad (12)$$

Solve the equations to find the camera's internal parameters $M = \begin{bmatrix} q_x & 0 & u_0 \\ 0 & q_y & v_0 \\ 0 & 0 & 1 \end{bmatrix}$.

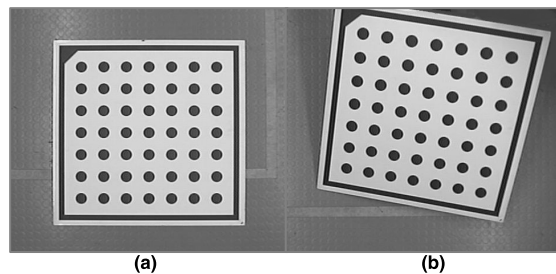


FIGURE 15. Calibration plate image. (a) angle 1. (b) angle 2.

According to the obtained homography matrix H and the internal parameter M , the external parameter O of the camera can be obtained:

$$\begin{cases} r_1 = \mu M^{-1}h_1 \\ r_2 = \mu M^{-1}h_2 \\ r_3 = r_1 \times r_2 \\ T = \mu M^{-1}h_3 \end{cases} \quad (13)$$

where r_1, r_2 and r_3 are the rotation vectors, T is the translation vector.

Camera calibration needs to be realized by an image with a calibration plate. The more calibration images obtained, the higher the accuracy of the internal parameters of the camera. In this paper, 12 calibration plate images are selected for calibration. The 30*30 calibration plate image used in this paper is shown in Figure 14. It contains 49 circular markers, the center point of each circular marker is the marker point. Figures 15(a) and (b) are two different angle calibration plate images. The specific calibration process is as follows: Firstly, the camera internal parameters are initialized according to the lens specification, and the world coordinates of the marker points are obtained from the calibration plate description file. Then 12 calibration plate images are sequentially read, and the image coordinates and initial external parameters of the marker points are searched. Finally, the world coordinates of the marker points, the image coordinates of the marker points in the 12 images, the initial internal parameters, and the initial external parameters of the 12 images are used to obtain the final internal and external parameters, which are the camera parameters obtained after calibration.

B. AXIS FITTING OF THE INSULATOR STRING

Taking the right insulator string in Figure 14(a) as an example, the coordinates of the left and right boundary points of each insulator are separately searched. The pixel coordinates of the center points can be calculated and converted into world coordinates by the camera calibration parameters. The calculation results are shown in Table 3. The numbers 1-11 respectively represent 11 insulators from the top to the bottom of the right insulator string in Figure 14(a), and the world coordinates of the center points of each insulator can be calculated in turn.

These central data points are fitted by least square method (LSM) [32]. Finding the line $y = a+bx$ whose sum of squares

TABLE 3. Center point coordinate calculation.

Number	Left boundary point/pixel	Right boundary point/pixel	Center point coordinate	
			Pixel coordinate/pixel	World coordinate/m
1	(426,-4)	(454,-10)	(440,-7)	(0.174459,-0.761196)
2	(414,-15)	(455,-25)	(434.5,-20)	(0.160096,-0.796238)
3	(417,-25)	(445,-36)	(431,-30.5)	(0.15098,-0.824642)
4	(396,-35)	(456,-52)	(426,-43.5)	(0.137908,-0.859915)
5	(411,-54)	(457,-61)	(424,-57.5)	(0.132805,-0.89809)
6	(400,-65)	(439,-77)	(419.5,-71)	(0.121034,-0.935021)
7	(401,-79)	(431,-87)	(416,-83)	(0.111883,-0.967984)
8	(382,-88)	(439,-106)	(410.5,-97)	(0.0974041,-1.00659)
9	(396,-105)	(422,-112)	(409,-108.5)	(0.0935487,-1.03846)
10	(385,-117)	(423,-127)	(404,-172)	(0.0809896,-1.07686)
11	(385,-130)	(414,-137)	(399.5,-133.5)	(0.0684264,-1.10814)

of distance from the given point (x_i, y_i) is the smallest:

$$\sum_{i=1}^N [y_i - (a + bx_i)]^2 = \min \tag{14}$$

The partial derivatives of a and b are obtained respectively:

$$\begin{cases} \frac{\partial}{\partial a} \sum_{i=1}^N [y_i - (a + bx_i)]^2 = -2 \sum_{i=1}^N (y_i - a - bx_i) = 0 \\ \frac{\partial}{\partial b} \sum_{i=1}^N [y_i - (a + bx_i)]^2 = -2 \sum_{i=1}^N [y_i - (a + bx_i)] x_i = 0 \end{cases} \tag{15}$$

Get the equations:

$$\begin{cases} aN + b \sum x_i = \sum y_i \\ a \sum x_i + b \sum x_i^2 = \sum x_i y_i \end{cases} \tag{16}$$

The best estimate of the linear parameters a and b can be obtained by solving the above equations:

$$\begin{cases} \hat{a} = \frac{(\sum x_i^2)(\sum y_i) - (\sum x_i)(\sum x_i y_i)}{N(\sum x_i^2) - (\sum x_i)^2} \\ \hat{b} = \frac{N(\sum x_i y_i) - (\sum x_i)(\sum y_i)}{N(\sum x_i^2) - (\sum x_i)^2} \end{cases} \tag{17}$$

The fitting linear equation $y = a + bx$ can be obtained. The result of fitting to the world coordinates of center points in Table 3 is shown in Figure 16, red indicates the fitted line, and the function is $y = -1.349 + 3.43 x$.

C. DEVIATION ANGLE AND DISTANCE CALCULATION

(1) Calculate deviation angle: According to the slope of $y = -1.349 + 3.43 x$, the angle between the insulator string and the horizontal line can be calculated as 73.746° , and the deviation angle is obtained $\theta = 16.254^\circ$.

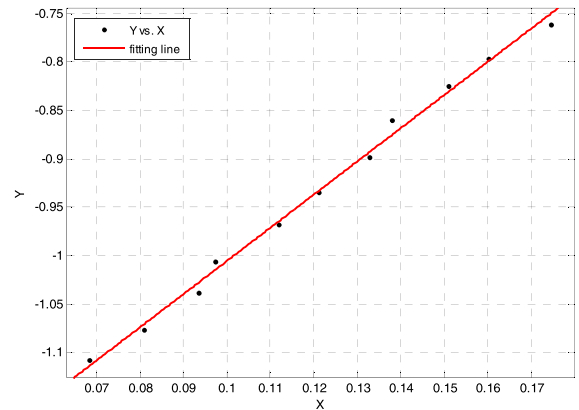


FIGURE 16. Fitting of the right insulator string.




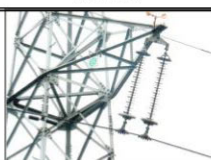

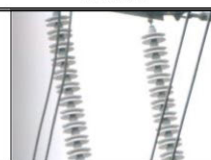
(2) The projection point of the first center point on the fitted line is $(0.174459, -0.7506)$, and the projection point of the last center point on the fitted line is $(0.0684264, -1.1143)$, and the length of the insulator string can be calculated $L = \sqrt{(x_1 - x_2)^2 + (y_1 - y_2)^2} \approx 378.8\text{mm}$, the deviation distance $d = 106.026\text{mm}$.

Similarly, the coordinates of the center points of the left insulator string in Figure 14(a) are transformed and fitted. The result is shown in Figure 17. The fitting line is $y = 0.1648 + 3.449x$, and the deviation angle can be calculated $\theta = 16.169^\circ$, the value deviation distance can be calculated $d = 41.325\text{mm}$.

V. FIELD ANALYSIS AND VERIFICATION

In [33], by extracting the coordinates of two end points of the insulator string, the calculation of wind deviation of the insulator string is realized according to the camera measurement model. Several field insulator string images of different transmission lines are selected as the research object.

TABLE 4. Deviation angle and distance calculation results.

Single insulator string				
This paper	Deviation angle/ ^o	13.068	3.481	8.927
	Deviation distance/mm	103.377	152.491	80.660
Reference [33]	Deviation angle/ ^o	13.066	3.358	8.917
	Deviation distance/mm	103.258	153.480	79.664
Manual method	Deviation angle/ ^o	14.2	3.6	9.3
	Deviation distance/mm	105.5	150.4	82.3
Relative error 1 /%	Angle/distance	7.97/2.01	3.31/1.39	4.01/1.99
Relative error 2 /%	Angle/distance	7.99/2.13	6.72/2.05	4.12/3.20
Operating state		Normal	Normal	Normal
Double insulator string				
This paper	Deviation angle/ ^o	Left: 13.598 Right: 11.593	Left: 3.725 Right: 13.799	Left: 6.621 Right: 8.386
	Deviation distance/mm	Left: 367.982 Right: 336.181	Left: 177.504 Right: 328.917	Left: 232.734 Right: 253.651
Reference [33]	Deviation angle/ ^o	Left: 13.070 Right: 11.432	Left: 3.516 Right: 12.881	Left: 6.555 Right: 8.448
	Deviation distance/mm	Left: 367.536 Right: 335.216	Left: 179.010 Right: 329.875	Left: 232.715 Right: 252.925
Manual method	Deviation angle/ ^o	Left: 14.6 Right: 12.7	Left: 3.9 Right: 14.2	Left: 6.9 Right: 8.3
	Deviation distance/mm	Left: 372.4 Right: 339.6	Left: 173.0 Right: 325.3	Left: 235.8 Right: 256.3
Relative error 1 /%	Angle/distance	Left: 6.86/1.19 Right: 8.72/1.01	Left: 4.49/2.60 Right: 2.82/1.11	Left: 4.04/1.30 Right: 1.04/1.03
Relative error 2 /%	Angle/distance	Left: 10.48/1.31 Right: 9.98/1.29	Left: 9.85/3.47 Right: 9.29/1.41	Left: 5.00/1.31 Right: 1.78/1.32
Operating state		Left: Alarm Right: Alarm	Left: Normal Right: Alarm	Left: Normal Right: Normal

Measuring the deviation angle and distance of the insulator string by the proposed method in this paper, [33] and manual method, the results are shown in Table 4.

The relative error 1 represents the relative error between the proposed method and the manual method, and the relative error 2 represents the relative error between the [33] and the manual method. By comparing the measurement results and the relative errors of this three methods, all the relative errors 1 are smaller than the relative errors 2. Moreover, for the deviation angle, the maximum and minimum errors of the proposed method are 8.72% and 1.04%, which are smaller than the [33] (10.48% and 1.78%). For the deviation distance, the maximum and minimum errors of the proposed method

are 2.60% and 1.01%, which are also smaller than the [33] (3.47% and 1.29%). It is verified that the measurement accuracy of the proposed method in this paper is higher than the [33]. When the deviation angle of the suspension insulator string is greater than 7.5° and the deviation distance is greater than 300mm, an alarm will be given to remind the staff to make corresponding maintenance. Otherwise, it indicates that the insulator string operates normally. The operating states of the field insulator images are shown in Table 4. The operating states of the single insulator string are all normal, which of the double insulator string consist of normal and alarm. It conforms to the actual operating state of insulators.

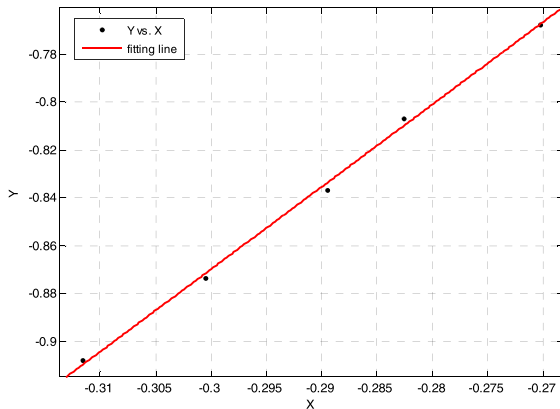


FIGURE 17. Fitting of the left insulator string.

TABLE 5. Identification accuracy of field images.

Image	Number	Identification accuracy/%
Single insulator string	100	93.75
Double insulator string	100	91.36

In addition, this paper selects 200 field insulator images for analysis, which contains 100 single insulator string images and 100 double insulator string images. The identification results of the operation state are shown in Table 5, the identification accuracy are 93.75% and 91.36% respectively, which shows that the accuracy of the single insulator string is higher than the double insulator string. To sum up, the proposed method is effective and practical.

VI. CONCLUSION

A technology of actual wind deviation monitoring for suspension insulator strings based on improved edge detection is proposed in this paper, which uses the video monitoring device to collect the image of the insulator string, and the image processing technology to extract the insulator target and characteristic parameters. Firstly, an improved gray-scale method is proposed to improve the contrast between the insulator and the background. Then, an improved Kirsch operator is proposed to obtain the complete single-pixel wide insulator string edge. The center point of each insulator is calculated and fitted. Finally, by calculating the relative error and comparing with the [33], the maximum and minimum errors of this paper are 8.72% and 1.01% respectively, which are smaller than the [33]. And by analyzing 200 field insulator images, the identification accuracy are 93.75% and 91.36%, which verified that the proposed method is effective and practical. Our future works are as follows: on the one hand, we will continue to simplify the design and structure of the monitoring device; on the other hand, collecting more insulator images under different field conditions for analysis, and optimizing the pre-processing, segmentation, edge detection, feature extraction algorithms continuously. And improving the performance and the accuracy of the wind deviation analysis algorithms.

REFERENCES

- [1] M. M. Hussain, S. Farokhi, S. G. McMeekin, and M. Farzaneh, "Mechanism of saline deposition and surface flashover on outdoor insulators near coastal areas part II: Impact of various environment stresses," *IEEE Trans. Dielectr. Electr. Insul.*, vol. 24, no. 2, pp. 1068–1076, Apr. 2017.
- [2] Y. Lu, H. Liu, C. Hu, C. Luo, Z. Zhou, and F. Tao, "A three-dimensional real-time model for calculating minimum air clearance on wind deviation of overhead transmission line," in *Proc. 2nd Int. Conf. Power Renew. Energy (ICPRE)*, Chengdu, China, Sep. 2017, pp. 276–280.
- [3] Y. Wu, B. Jiang, and N. Lu, "A descriptor system approach for estimation of incipient faults with application to high-speed railway traction devices," *IEEE Trans. Syst., Man, Cybern., Syst.*, vol. 49, no. 10, pp. 2108–2118, Oct. 2019.
- [4] Y. Wu, B. Jiang, and Y. Wang, "Incipient winding fault detection and diagnosis for squirrel-cage induction motors equipped on CRH trains," *ISA Trans.*, 2019, doi: 10.1016/j.isatra.2019.09.020.
- [5] Z. Li, G. Wu, and Z. Wang, "Windage yaw disaster monitoring and early warning technology based on power micrometeorological and system implementation," *Power Syst. Protection Control*, vol. 45, no. 1, pp. 125–131, Jan. 2017.
- [6] C. Li, X. Li, X. Peng, H. Zhang, C. Wang, S. Fan, and S. Cao, "Analyzing the applicability of side-polished fiber Bragg grating tilt sensor using liquid pendulum with controllable angle," in *Proc. IEEE SENSORS*, Glasgow, U.K., Oct./Nov. 2017, pp. 1–3.
- [7] Z. Tang, Z. Liao, and X. Yuan, "Analysis of influence factors on computing wind deflection angle with rigid body straight rod model," *Insulators Surge Arresters*, no. 3, pp. 208–212, Jun. 2018.
- [8] R. C. Gonzalez and R. E. Woods, *Digital Image Processing*. Upper Saddle River, NJ, USA: Prentice-Hall, 2000, pp. 103–113.
- [9] X. Huang, T. Nie, Y. Zhang, and X. Zhang, "Study on hydrophobicity detection of composite insulators of transmission lines by image analysis," *IEEE Access*, vol. 7, pp. 84516–84523, 2019.
- [10] F. Luo, B. Du, L. Zhang, L. Zhang, and D. Tao, "Feature learning using spatial-spectral hypergraph discriminant analysis for hyperspectral image," *IEEE Trans. Cybern.*, vol. 49, no. 7, pp. 2406–2419, Jul. 2019.
- [11] L. Zhang, L. Zhang, B. Du, J. You, and D. Tao, "Hyperspectral image unsupervised classification by robust manifold matrix factorization," *Inf. Sci.*, vol. 485, pp. 154–169, Jun. 2019.
- [12] H. Chen, "Application of GPRS communication technology in distribution network automation monitoring system," M.S. thesis, Shandong Univ., Jinan, China, Apr. 2006.
- [13] X. B. Huang, F. Zhang, H. Li, and X. Liu, "An online technology for measuring icing shape on conductor based on vision and force sensors," *IEEE Trans. Instrum. Meas.*, vol. 66, no. 12, pp. 3180–3189, Dec. 2017.
- [14] H. Y. Li, "Discussion on operation management and optimization countermeasures of UHV transmission lines," *Technol. Innov. Appl.*, no. 36, pp. 100–101, 2017.
- [15] J. P. Wang and Z. L. Luo, "Operation and maintenance management strategy of 500 kV UHV transmission lines," *Commun. world*, no. 14, pp. 247–248, Jul. 2017.
- [16] J. Lin, J. Han, F. Chen, X. Xu, and Y. Wang, "Defects detection of glass insulator based on color image," *Power Syst. Technol.*, vol. 35, no. 1, pp. 127–133, 2011.
- [17] H.-R. Jiang, L.-J. Jin, and S.-J. Yan, "Recognition and fault diagnosis of insulator string in aerial images," *J. Mech. Elect. Eng.*, vol. 32, no. 2, pp. 274–278, 2015.
- [18] I. Ahmad, I. Moon, and S. J. Shin, "Color-to-grayscale algorithms effect on edge detection—A comparative study," in *Proc. Int. Conf. Electron., Inf., Commun. (ICEIC)*, Honolulu, HI, USA, Jan. 2018, pp. 1–4.
- [19] F. Huang, Q. Yu, X. Yao, G. Shang, Y. Zhu, Y. Wu, and Y. Huang, "K-means clustering segmentation for H weight of wheat canopy image," *Comput. Eng. Appl.*, vol. 50, no. 3, pp. 129–134, 2014.
- [20] X. B. Huang, X. H. Liu, and Y. Zhang, "Classification recognition method of insulator in aerial image based on the red-blue difference and developed K-means algorithm," *High Voltage Eng.*, vol. 44, no. 5, pp. 1528–1534, May 2018.
- [21] W. Shan, Y. Yi, J. Qiu, and A. Yin, "Robust median filtering forensics using image deblocking and filtered residual fusion," *IEEE Access*, vol. 7, pp. 17174–17183, 2019.
- [22] K. H. Rhee, "Forensic detection using bit-planes slicing of median filtering image," *IEEE Access*, vol. 7, pp. 92586–92597, 2019.

- [23] J. Chen, B. Guan, H. Wang, X. Zhang, Y. Tang, and W. Hu, "Image thresholding segmentation based on two dimensional histogram using gray level and local entropy information," *IEEE Access*, vol. 6, pp. 5269–5275, 2017.
- [24] J. Sivakamasundari, G. Kavitha, V. Natarajan, and S. Ramakrishnan, "Proposal of a content based retinal image retrieval system using kirsch template based edge detection," in *Proc. Int. Conf. Inform., Electron. Vis. (ICIEV)*, Dhaka, Bangladesh, May 2014, pp. 1–5.
- [25] L. Zhang, "Image edge detection based on Kirsch operator," M.S. thesis, Northeast Petroleum Univ., Daqing, China, 2014.
- [26] Y. Zhang, H. Jiang, D. Zhu, and Z. Wang, "Human contour extraction based on skeleton matching," *J. Syst. Simul.*, vol. 29, no. 11, pp. 2774–2781, Nov. 2017.
- [27] Z. H. Diao, B. B. Wu, Y. Y. Wu, and Y. Q. Wei, "Application research of skeleton extraction algorithm based on image processing," *Comput. Sci.*, vol. 43, no. 6A, pp. 232–235, Jun. 2016.
- [28] X. Huang, L. Yang, Y. Zhang, Y. Zhu, and G. Zhang, "A measurement technology of space distance among transmission bundle conductors based on image sensors," *IEEE Trans. Instrum. Meas.*, vol. 68, no. 10, pp. 4003–4014, Oct. 2019.
- [29] C. H. Yu and L. Y. Qi, "Binocular camera calibration based on HALCON," *Elect. Des. Eng.*, vol. 25, no. 19, pp. 190–193, Oct. 2017.
- [30] Y. Liao, G. Li, Z. Ju, H. Liu, and D. Jiang, "Joint Kinect and multiple external cameras simultaneous calibration," in *Proc. 2nd Int. Conf. Adv. Robot. Mechatronics (ICARM)*, Feb. 2018, pp. 305–310.
- [31] A. Fetić, D. Jurić, and D. Osmanković, "The procedure of a camera calibration using camera calibration toolbox for MATLAB," in *Proc. 35th Int. Conv. MIPRO*, May 2012, pp. 1752–1757.
- [32] L. Liu, Y. Liu, and Y. Tang, "Study on duration calculate model of railway construction based on LSM," in *Proc. Int. Conf. Logistics, Informat. Service Sci. (LISS)*, Jan. 2016, pp. 1–5.
- [33] T. T. Guo, "Research on the detection of transmission line windage yaw based on video monitoring," M.S. thesis, Xihua Univ., Chengdu, China, 2016.



XINBO HUANG (SM'16) was born in Shandong, China, in 1975. He received the B.S. and M.S. degrees in automation from Qingdao Technological University, Qingdao, China, in 1998 and 2001, respectively, and the Ph.D. degree in automation from Xidian University, Xi'an, China, in 2005. He is currently a Professor with the School of Electronics Information, Xi'an Polytechnic University, Xi'an, and also a Ph.D. Supervisor with the School of Electro-Mechanical Engineering, Xidian University. His current research interests include the online monitoring technology, the image recognition technology, and the wireless network sensor.



YE ZHANG was born in Shaanxi, China, in 1988. She received the B.S. and M.S. degrees in electronic information engineering from Xi'an Polytechnic University, Xi'an, China, in 2011 and 2014, respectively. She is currently pursuing the Ph.D. degree in electro-mechanical engineering with Xidian University, Xi'an. Her main research interests include intelligent power and online monitoring technology.



LUYA YANG was born in Shanxi, China, in 1993. She received the B.S. and M.S. degrees in electronic information engineering from Xi'an Polytechnic University, Xi'an, China, in 2016 and 2019, respectively. She is currently pursuing the Ph.D. degree with the School of Electro-Mechanical Engineering, Xidian University, Xi'an. Her current research interest includes fault detection based on image processing.



TINGTING NIE was born in Henan, China, in 1995. She received the B.S. degree from the College of Information and Business, Zhongyuan University of Technology, Zhengzhou, China, in 2018. She is currently pursuing the M.S. degree with Xi'an Polytechnic University, Xi'an, China. Her current research interest includes water-based detection based on image processing.

...